1-30-2023

Nanoscale Hafnium Metal-organic Frameworks Enhance Radiotherapeutic Effects by Upregulation of Type I Interferon and TLR7 Expression

Eunseo Choi
Oregon State University

Madeleine R. Landry
Oregon State University

Nathan Pennock
Oregon Health & Science University

Katherine Weinfurter
Portland State University

multiple additional authors

Citation Details

Published as: Choi, E., Landry, M., Pennock, N., Neufeld, M., Weinfurter, K., Goforth, A., ... & Sun, C. (2023). Nanoscale Hafnium Metal-organic Frameworks Enhance Radiotherapeutic Effects by Upregulation of Type I Interferon and TLR7 Expression. Advanced Healthcare Materials, 2202830.

Nanoscale hafnium metal-organic frameworks enhance radiotherapeutic effects by upregulation of type I interferon and TLR7 expression

*Eunseo Choi, Madeleine Landry, Nathan Pennock, Megan Neufeld, Katherine Weinfurter, Andrea Goforth, Joshua Walker, and Conroy Sun**

E. Choi, M. Landry, M. Neufeld, C. Sun

Department of Pharmaceutical Sciences

College of Pharmacy

Oregon State University

Portland, OR 97201, USA

E-mail:sunc@ohsu.edu

J. Walker, N. Pennock, C. Sun

Department of Radiation Medicine

This article has been accepted for publication and undergone full peer review but has not been through the copyediting, typesetting, pagination and proofreading process, which may lead to differences between this version and the Version of Record. Please cite this article as doi: 10.1002/adhm.202202830.

WILEY-VCH

School of Medicine

Oregon Health & Science University

Portland, OR 97201, USA

J. Walker, N. Pennock

Department of Cell, Developmental, and Cancer Biology

School of Medicine

Oregon Health & Science University

Portland, OR 97201, USA

K. Weinfurter, A. Goforth

Department of Chemistry

Portland State University

Portland, OR 97201, USA

WILEY-VCH

Keywords: folate, Imiquimod, DNA damage, cell death, IRF activation, T cell proliferation

Recent preclinical and clinical studies have highlighted the improved outcomes of combination radiotherapy and immunotherapy. Concurrently, the development of high-Z metallic nanoparticles as radiation dose enhancers has been explored to widen the therapeutic window of radiotherapy and potentially enhance immune activation. In this study, we evaluate folate-modified hafnium-based metal-organic frameworks (HfMOF-PEG-FA) in combination with imiquimod, a TLR7 agonist, as a well-defined interferon regulatory factor (IRF) stimulator for local antitumor immunotherapy. The enhancement of radiation dose deposition by HfMOF-PEG-FA and subsequent generation of reactive oxygen species (ROS) deregulates cell proliferation and increases apoptosis. HfMOF-PEG-FA loaded with imiquimod (HfMOF-PEG-FA@IMQ) increases DNA double-strand breaks and cell death, including apoptosis, necrosis, and calreticulin exposure, in response to X-ray irradiation. Treatment with this multipronged therapy promotes IRF stimulation for subsequent interferon production within tumor cells themselves. We report the novel observation that, HfMOF itself increased TLR7 expression, unexpectedly pairing immune agonist and receptor up-regulation in a tumor intrinsic manner, and supporting the synergistic affect observed with the γH2AX assay. T cell analysis of CT26 tumors following intratumoral administration of HfMOF-PEG-FA@IMQ with radiotherapy reveals a promising antitumor response, characterized by an increase in CD8+ and proliferative T cells.

1. Introduction

The radiosensitization effects of high atomic number (high-Z) metal nanoparticles have been investigated in various cancer models to elucidate the physical radiation dose enhancement and altered radiobiological effects that result in improved radiotherapy.[1] Among the platforms that have been studied, hafnium (Hf)-based nanoparticles have recently attracted significant attention due to their unique biological and physiochemical properties.[2] In ongoing clinical trials, NBTXR3 (Nanobiotix), a functionalized and crystalline Hf oxide nanoparticle, demonstrates potential efficacy in various solid tumor treatments, including rectal, prostate, and head and neck squamous cell carcinomas.[3] In addition to NBTXR3, numerous preclinical studies of Hf-based nanoparticles, such as

Hf-doped hydroxyapatite nanoparticles and Hf-containing metal-organic frameworks (HfMOF), have shown good biocompatibility and synergistic antitumor effects with radiotherapy.[4] Furthermore, radiosensitization by Hf-nanoparticles has been investigated as a tool to elicit innate and adaptive immune responses.[5]

In radiotherapy, ionizing radiation (IR) kills cancer cells by forming reactive oxygen and nitrogen species that destroy biological macromolecules and cellular constituents. Nuclear DNA is one of the most radiosensitive cellular targets, in which IR causes cell lethality by increasing DNA double-strand breaks (DSBs).[6] Unrepaired DSBs affect cell survival and play a crucial role in determining cellular fate. Although Hf-nanoparticles are proposed to enhance radiotherapy through increased accumulation of DSBs, the practical application of these materials as radiosensitizers has been limited due to poorly understood radiation dose deposition and insufficient local ROS generation, as well as an unclear effect on tumor cell death mechanisms.[7] It has been suggested that Hf-nanoparticles, such as NBTXR3, may stimulate the cyclic GMP-AMP synthase (cGAS)-stimulator of interferon genes (STING) pathway as an immunotherapy for solid tumors typically treated with radiotherapy, including colorectal cancer (CRC).[8] Activation of the STING pathway initiates innate and adaptive immune responses in human CRC by upregulating type I interferon (IFN) genes, including interferon regulatory factor (IRF), nuclear factor-κB (NF-κB), and toll-like receptors (TLRs).[9] Unfortunately, while various STING agonists have demonstrated impressive potential in cancer immunotherapy, the majority of these compounds exhibited dose-limiting toxicities.[10] As such, the development of STING-targeted cancer therapies that avoid systemic adverse effects and maximize therapeutic efficacy remains challenging.[11] In the case of radiosensitizing nanoparticles, the increased induction of DSBs in the presence of IR and the

subsequent formation and persistence of micronuclei is directly linked to the activation of cGAS-STING innate immunity signaling pathway.[12]

An alternative approach is to combine radiosensitizing nanoparticles and immunostimulatory adjuvants, such as pathogen-associated molecular pattern/damage associated molecular pattern (PAMP/DAMP) receptor agonists, that engage either STING activation or type I IFN secretory pathways. Various TLR agonists are being investigated as immunostimulatory adjuvants for activating antigen-presenting cells and boosting immune responses.[13] TLR7 agonists, which include imiquimod (IMQ), are established immune stimulators having been shown to promote tumor regression of benign basal cell carcinoma and are being explored for applications in cancer therapeutic settings. These agonists have also been observed to act as autophagy promoters in human colonic adenocarcinoma cells and provide effective immune adjuvant properties when combined for local radiotherapy in melanoma and breast cancer.[14] Although TLR agonists have the potential to enhance cytotoxic chemotherapies and ionizing radiation, only a few studies have focused on DNA stress caused by these compounds.[15] Mechanistically, TLR7 engagement and therapeutic effect is associated with its direct activity within dendritic cells where it causes production and release of high amounts of type I IFNs in both humans and mice. This increased type I IFN production promotes anti-tumor immunity by engaging with surrounding T cells, enhancing cytotoxic T cell differentiation and increasing T cell survival.[16]

Consolidating these facets into one therapeutic agent, in this study, we formulated a nanoscale HfMOF and loaded it with IMQ to enhance CRC cell death and stimulate type I IFN signaling induced by IRF. We modified IMQ-loaded HfMOF with DSPE-PEG-folate (HfMOF-PEG-FA@IMQ) to target folate receptor-expressing CRC cells. The physical properties of HfMOF-PEG-

FA@IMQ, such as the hydrodynamic size, surface charge, and morphology, were determined. The radiosensitizing effect of HfMOF-PEG-FA was examined by real-time monitoring of the proliferative activity of CRC cells. DSBs caused by phosphorylated H2AX (γH2AX) were examined to evaluate the radiotherapeutic effect, and apoptotic/necrotic and immunogenic cell death was confirmed by staining the outer cell membrane exposed to translocated phosphatidylserine and calreticulin (CRT). IRF activation was quantitatively evaluated by measuring IRF transcriptional activity using a luciferase reporter assay. Finally, the *in vivo* efficacy of HfMOF-PEG-FA@IMQ with IR was evaluated by T cell analysis in mouse CRC tumors.

2. Results and Discussion

2.1. Characterization of HfMOF-PEG-FA@IMQ

HfMOF nanoparticles were synthesized using terephthalic acid (BDC), a secondary building unit, as described previously (Figure 1A).[17] The surface of HfMOF was physically modified with PEG using DSPE-PEG or DSPE-PEG-FA to improve hydrophilicity and cellular uptake by folate receptor-overexpressing CRC cells.[18] PEGylation of inorganic nanoparticles has been widely applied to increase water solubility and reduce plasma protein adsorption.[19] Using a conventional thin film hydration technique, HfMOFs were successfully PEGylated with the active ligand folate without aggregation or dissociation. Here the PEGylated phospholipid is employed as a biocompatible amphiphilic polymer that can stabilize hydrophobic HfMOFs and interact with the surrounding hydrophilic environment.[20] The size distribution and morphology of HfMOF and HfMOF-PEG-FA were examined by transmission electron microscopy (TEM) and dynamic light scattering (DLS). TEM

images of HfMOF showed an average measured size of 90.2 ± 12.5 nm (Figure 1B, left), while images of HfMOF-PEG-FA showed slight increase in size averaging 137.5 ± 41.7 nm (Figure 1B, right); both nanoparticle formulations were homogeneous and spherical in morphology. The hydrodynamic size of HfMOF measured by DLS was 172.0 ± 8.2 nm.

In this study, IMQ was integrated in the HfMOF formulation as an immunostimulatory adjuvant. While several TLR agonists have been suggested as effective cancer immunotherapy partners, IMQ was chosen because the TLR7 signaling pathway plays an important role in the production of type I IFN through IRF activation.[13b, 21] Unfortunately, the current generation of TLR7 agonists have been limited in cancer therapy because of issues such as systemic toxicity and weak therapeutic efficacy.[22] Imiquimod is currently FDA-approved for the topical treatment of actinic keratosis and basal cell carcinoma.[23] In this indication, the local application of the TLR7 agonist allows for tolerable doses avoiding safety issues. An orally administered small molecule-based TLR7 agonist was evaluated in HCV-infected patients; however, despite positive clinical outcomes, product development was halted due to an animal study that revealed toxicity when the drug was given on a daily basis.[24] Here, we seek to address a significant delivery challenge by utilizing a nanoscale drug carrier, HfMOF. Due to the hydrophobic properties of IMQ and HfMOF, HfMOF@IMQ was prepared under agitation in an ultrasonic water bath to disperse IMQ in the HfMOF solution, as previously employed for IMQ delivery with nanoscale carriers.[25] IMQ encapsulation was quantified by HPLC. Approximately 2.3% IMQ was loaded into HfMOF, and the IMQ concentration in HfMOF was 2.3 μg mg^{-1} (IMQ/HfMOF, w/w). IMQ is poorly soluble in most organic solvents. Despite the fact that loading efficiency remains somewhat low, the radiosensitizing activity of IMQ loaded HfMOFs could be quite significant when compared to other IMQ loaded nanoscale drug carriers. After loading IMQ

into HfMOF-PEG and HfMOF-PEG-FA, the DLS diameters of HfMOF-PEG@IMQ and HfMOF-PEG-FA@IMQ were 195.8 ± 24.5 and 183.8 ± 1.8 nm resulting in a slight increase in size (Figure 1C). The surface charge of HfMOF was + 48.8 ± 3.7 mV and significantly decreased to + 25.8 ± 3.7 mV after IMQ loading. The surface charge measurement might be influenced by sequential washing steps and adsorption of IMQ on the HfMOF surface. (Figure S1, Supporting Information)

After further modification of HfMOF@IMQ with DSPE-PEG or DSPE-PEG-FA, surface charges of HfMOF-PEG@IMQ and HfMOF-PEG-FA@IMQ were + 4.3 ± 3.8 and -13.2 ± 15.2 mV, respectively, indicating that successful PEGylation reduced the cationic charge of HfMOF (Figure 1D). The FT-IR spectra of HfMOF-PEG-FA showed a strong peak at 1390 cm^{-1}, due to the bridging carboxylate groups of BDC, even after IMQ and PEG modification (Figure 1E). The peaks at 1440 cm^{-1} (CH_2 bending) and 1570 cm^{-1} (C=C stretching) increase in intensity with the addition of DSPE-PEG or DSPE-PEG-FA, which supports their presence on the surface of the HfMOF. The powder X-ray diffraction (XRD) pattern showed that HfMOF had a crystal structure identified as UiO-66-type with face-centered cubic (fcc) topography (Figure 1F). The same open framework crystal structure is observed after the addition of IMQ, DSPE-PEG, and DSPE-PEG-FA, as demonstrated by both XRD and FT-IR analysis. (Figure S2, Supporting Information) Collectively these observations demonstrate; successful encapsulation of IMQ, consistent modification of the HfMOF with physiochemical properties useable for *in vivo* applications and that inclusion of IMQ does not result in increased variability or negatively impact these important features.

2.2. HfMOF radiosenstization and TLR7 expression

Previous *in vitro* studies of Hf oxide nanoparticles have demonstrated increased energy dose deposition in irradiated cells.[3a, 26] Before determining the radiotherapeutic effects of HfMOF-PEG-FA, we first examined cellular uptake of Hf in human colon cancer, HCT116, cells using inductively coupled plasma mass spectrometry (ICP-MS). Hf accounted for approximately 50% of the total weight of the HfMOF-PEG and HfMOF-PEG-FA formulations. The intracellular uptake of Hf in HCT116 was approximately 2.8-fold higher in HfMOF-PEG-FA-treated cells than in HfMOF-PEG-treated cells after 4 h (Figure S3, Supporting Information). HfMOF-PEG-FA was more efficiently internalized into cells than HfMOF-PEG due to the high binding affinity of folic acid for the folate receptor that is overexpressed on the surface of CRC cells (the bottom of Figure S3). As for folate targeting, cytotoxicity of HfMOF-PEG-FA in folate receptor deficient HCT116, NIH3T3, and HEK293T cells showed consistent results with our design to increase uptake of HfMOF through folate modification. (Figure S6, Supporting Information)

Next, to evaluate the radiotherapeutic effects of HfMOF and determine whether inclusion of IMQ altered the radiotherapeutic effects of HfMOF, we analyzed DNA damage-induced cancer cell death. First, we detected DSBs by staining γH2AX in the nucleus. The fluorescence intensity of eFluor 660, which represents γH2AX foci, was visualized by fluorescence microscopy at 2 h after irradiation (Figure 2A). We observed more significant DNA damage in γH2AX puncta induced by HfMOF-PEG-FA@IMQ at 2 and 4 Gy. The number of γH2AX foci per cell irradiated at 4 Gy with free IMQ, HfMOF-PEG-FA, and HfMOF-PEG-FA@IMQ was calculated as 36.5 ± 6.5, 40.8 ± 7.6, and 59.8 ± 9.7,

respectively, after quantifying via CellProfiler analysis (Figure 2B). HfMOF-PEG-FA@IMQ with 4 Gy caused 1.5 times more DNA damage than IMQ or HfMOF-PEG-FA. This enhanced IR-induced cellular damage was observed in even lower doses at 2 Gy, exhibiting a 2.2- and 1.4-fold increase in DNA damage after HfMOF-PEG-FA@IMQ treatment compared to IMQ or HfMOF-PEG-FA, respectively.

γH2AX imaging showed synergistic therapeutic effects of HfMOF-PEG-FA@IMQ, indicating that intact IMQ may be delivered into cells to either enhance the generation of DSBs or inhibit DSB repair. These results were surprising given most TLR7 expression on cancer cells is low or absent, and generally TLR7 agonist anti-tumor activity is ascribed to TLR7 high expressing dendritic cells. The increased γH2AX foci in HfMOF-PEG-FA, with and without IR or IMQ in HCT116 suggested that HfMOF-PEG-FA itself may upregulate TLR7 expression. To pursue this possibility, we examined the TLR7 expression levels in HCT116 (Figure 2C) with and without HfMOF-PEG-FA treatment. Western blot showed that HfMOF-PEG-FA upregulated 2-fold more TLR7 expression compared with PBS control in HCT116. This result supports a previously unreported effect of HfMOF-PEG-FA and provides a mechanistic underpinning for the tumor cell intrinsic observation of synergistic γH2AX signal from the combination of HfMOF-PEG-FA with IMQ.

2.3. CRC cell death by radiotherapy

To further evaluate HfMOF-PEG-FA as a radiosensitizer, we examined proliferation and apoptotic induction in HCT116 cells. Here we performed a clonogenic cell survival assay after treatment with HfMOF-PEG-FA and IR at various radiation doses (Figure 2D). At 1 Gy, there was no severe inhibition of clonogenic survival in comparison to control cells. However, IR at 2 Gy resulted in a 2-fold

reduction of survival fraction (%) compared to no treatment, 7.8 ± 1.1% for HfMOF-PEG-FA. HfMOF-PEG-FA radio-sensitized HCT116 cells as the IR dose increased from 1 to 3 Gy. At doses higher than 4 Gy, untreated cells exhibited a 1% survival fraction, whereas HfMOF-PEG-FA treated cells formed no colonies. Controlled cancer cell growth might be linked to either reduced rates of proliferation and/or a high rate of cell death, as oncogenes target both of these pathways. To confirm irradiation-induced cell death, we stained cells with Annexin V and propidium iodide (PI) to investigate cell death stages and determine whether dying cells promoted apoptosis and necrosis when irradiated and treatment with HfMOF-PEG-FA@IMQ. As shown in Figure 2D, the control cells exhibited IR induced cell death as dose increased from 0 to 4 Gy (Figure 3A) 48 h after IR. Cells irradiated at 4 Gy with HfMOF-PEG-FA showed an increase in both early apoptotic cells (34.2 ± 1.6%, apoptosis) and late apoptotic/necrotic cells (37.8 ± 3.7%, late apoptosis/necrosis, Figure 3A). Overall, HfMOF-PEG-FA significantly induced higher levels of cell death for both 2 and 4 Gy irradiation than either radiation or HfMOF-PEG-FA alone. Consistent with previous findings, these results demonstrate that HfMOF-PEG-FA increases the radiosensitivity of tumor cells inducing greater tumor cell death at least in part through promotion of apoptosis and necrosis. In addition, these data validate that inclusion of IMQ does not hinder the radiosensitizing effect of HfMOF-PEG-FA.

Under particular conditions of tumor treatment, IR has been reported as an inducer of immunogenic cell death. Activation of the immune response by radiation can be in the form of induced release of cytokines or expression/release of endogenous DAMPs. Engagement with DAMP receptors on neighboring immune cells, signals a perturbation from homeostasis, mobilizing an innate immune response, which can culminate in triggering anti-tumor immunity.[27] Immunogenic cell death pathways have been characterized to actively shuttle the intracellular protein CRT to the

cell surface, which in turn promotes tumor cell phagocytosis by macrophages and dendritic cells and propagation of inflammatory signals.[28] In Figure 3B, cell surface exposure of CRT was much more prominent in irradiated and HfMOF-PEG-FA@IMQ-treated cells than either group alone. Higher surface CRT expression suggested that combining IMQ with HfMOF-PEG-FA could be a practical immunotherapeutic approach to facilitate not only apoptosis but also additional immunogenic forms of cell death for a synergistic antitumor immune response.

2.4. Type I IFN pathway activation

Upon observation of a synergistic increase in γH2AX expression with HfMOF-PEG-FA@IMQ, we postulated what impact of either enhanced DSB or delayed DSB repair may have on downstream immune activation signaling within cancer cells.[29] Unlike many other PAMPs/DAMPs, cGAS recognizes both endogenous and foreign cytoplasmic DNA elements as inducers of type I IFN signaling. Excess, persistent or unrepaired DNA damage is frequently shuttled out of the nucleus and into the cytoplasm either as micronuclei or free genomic material, where it can interact with cGAS and act as DAMP ligand.[30] Classical activation of cGAS results in activation of the STING and TANK-binding kinase 1 (TBK1) signaling pathways, which culminate in IRF and NF-κB activation.[31] Both IRF3 and IRF7 are key regulators in the production of type I IFN which has been strongly implicated as the chief mediator of radiotherapy induced immunogenicity.[8a, 32] Extensive prior research has demonstrated that when TLR7 is activated, dendritic cells produce a substantial amount of type I IFNs through an IRF mediated pathway, although the effects of TLR7 engagement on cancer cells have yet to be thoroughly investigated.[16, 33] We hypothesized that HfMOF-PEG-FA@IMQ could act

as an IR-sensitive type I IFN inducer via two different mechanisms (cGAS-STING or TLR7 activation), as described in Scheme 1, after observing increased DNA damage and cell death in CRC cells because the formation of micronuclei is correlated to the activation of cGAS-STING pathway. [30]

To evaluate the type I IFN inducing capacity of HfMOF-PEG-FA, we used HCT116-Dual (Invivogen) cells, a human colorectal carcinoma cell line expressing the luciferase gene under the ISG54 minimum promoter combined with five IFN-stimulated response elements and B16-Blue ISG (Invivogen) cells, an IRF inducible secreted embryonic alkaline phosphatase reporter B16 melanocytes used for the activation of the TBK1/IRF3 pathway by cytosolic DNA or cytosolic dinucleotides.[34] The luminescence signal released by HCT116-Dual cells and B16-Blue cells were monitored to measure IRF promoter activity using the reporter gene assay (Figure 4 and Figure S7). The expression level of luciferase and alkaline phosphatase were quantitatively measured by mixing luciferin-based luminescence reagent and colorimetric enzyme assay reagent with the cultured supernatant. Figure 4A shows that IR-activated cells increased IFN production in a radiation dose-dependent manner with a 1.9- and 2.4-fold increase 96 h after irradiation at 2 and 4 Gy, respectively. However, activation of the IFN response was not detected in IFN receptor-blocking HCT116 cells. (Figure 4B) When 4 Gy radiation was combined with HfMOF-PEG-FA the signal from type I IFN production was significantly higher than 4 Gy radiation alone. Interestingly, IMQ on its own generated no enhancement of type I IFN response. However, when combined with HfMOF-PEG-FA, type I IFN production was noticeably potentiated when the HfMOF-PEG-FA@IMQ concentration was 125.0 μg mL^{-1} with irradiation at 4 Gy, demonstrating an approximately 3.5-fold increase in IRF stimulation 1.5 times higher than the effect observed after irradiation at 4 Gy alone. To verify that HfMOF-PEG-FA@IMQ stimulates IRF-mediated type I IFN activation, B16-Blue cells were treated with

various concentrations of IMQ, HfMOF-PEG-FA, and HfMOF-PEG-FA@IMQ in the presence or absence of IFN receptor inhibitor. (Figure S7A and B) B16-Blue cells treated with HfMOF-PEG-FA@IMQ demonstrated increased IRF reporter activity as IR dose and concentration of Hf increased, but it was not stimulated in IFN receptor blocked B16-Blue cells.

2.5. CD8 T cell activation in murine model

To examine the combined impact of IMQ and HfMOF-PEG-FA on promoting both intrinsic radiosensitivity and immunological response, HfMOF-PEG-FA@IMQs were intratumorally administered to CT26 tumor-bearing BALB/c mice. Consistent with our earlier results in the human CRC cell lines, we observed that folate receptors were overexpressed on murine CT26 cells and that internalized Hf was higher in HfMOF-PEG-FA-treated cells in than HfMOF-PEG-treated cells (Figure S4, Supporting Information). To evaluate the radiosensitizing activity of HfMOF-PEG-FA on CT26 cells, the *in vitro* proliferative capacity of CT26 cells was evaluated using quantitative real-time live imaging of cell phase confluence. The proliferative ability was significantly decreased in HfMOF-PEG-FA treated cells with IR (Figure 5A). Control cells reached approximately 95% confluence after 48 h with IR, while HfMOF-PEG and HfMOF-PEG-FA treated cells reached approximately 80% confluence. Cells treated with IR and HfMOF-PEG + IR exhibited approximately 70% confluence, whereas HfMOF-PEG-FA + IR showed approximately 50% confluence. As demonstrated in the human cell line, to confirm IR induced cell death, we stained CT26 cells with Annexin V and PI to determine cell death stages (Figure 5B). Like previous results, the control cells demonstrated IR induced cell death as the IR dose increased from 0 to 4 Gy. Also, cells irradiated at 4 Gy with HfMOF-PEG-FA@IMQ showed

the highest increase in early apoptosis of 32.00 ± 0.85% and late apoptosis/necrosis of 12.45 ± 1.29%, respectively. The synergistic effect of the combination of HfMOF-PEG-FA with IMQ on apoptosis and necrosis in murine and human CRC cells showed similar trends of IR-sensitive cell death. We also confirmed that HfMOF-PEG-FA elevated TLR7 expression in CT26 cells (Figure S5, Supporting Information). With the basic tumor intrinsic effects established *in vitro* for CT26, we next employed our *in vivo* system as shown in Figure 5C. In our previous study, HfMOF was evaluated in both short- and long-term toxicity for *in vivo* translation. We determined folate modified HfMOF remained intact in serum containing condition for up to 96 h. (Figure S8, Supporting Information). In this study, BALB/c mice were injected in the flank with syngeneic CT26 murine CRC and allowed to grow to an average size of 50 mm^2. HfMOF-PEG-FA@IMQs were then intratumorally administered to CT26 tumor-bearing BALB/c mice followed by 4 Gy IR. Tumor sizes and growth changes were monitored every two days (Figure S9, Supporting Information). We observed significant reduction in tumor growth when IR was applied in both the PBS and HfMOF-PEG-FA@IMQ treated groups. Interestingly, administration of the HfMOF-PEG-FA alone significantly reduced tumor growth, however this reduction was not further enhanced with the addition of IR. This is distinct from what was observed with HfMOF-PEG-FA@IMQ, which showed greater tumor reduction with IR than HfMOF-PEG-FA with 3 of the 4 mice having the smallest tumors observed in the entire study at day 7. Acute tumor size alone does not indicate induced immunological activity as increased infiltration of immune cells has been noted in many circumstances to results in tumor swelling, a phenomenon known clinically as pseudo-progression.

To determine whether HfMOF-PEG-FA with or without IMQ demonstrated unique immunological properties, we thoroughly analyzed immune cells composition from tumor, tumor

draining lymph nodes and tumor distal lymph nodes (Figure 5D-F). Using 15 parameter flow cytometric analysis and 24 different target cell populations we employ Euclidean hierarchical clustering to identify trends in our tumor immune cell compositions (Figure 5E). We observed IR induced immune cells patterns, that generally carried across all treatment groups (Figure 5E, green box), including the upregulation of CD8 T cell frequency (Figure 5D, left). We were most interested in alterations indicative of unique biology induced by the use of the HfMOF-PEG-FA and HfMOF-PEG-FA@IMQ (black box). We observed that HfMOF-PEG-FA@IMQs treatment increased the frequency of both CD4+ and CD8+ T cells (CD3) expressing Ki67+, a protein tightly associated with cells undergoing proliferation (Figure 5F). The proliferation marker increase is dependent on the IMQ loaded HfMOF-PEG-FA, despite the dose of IMQ being lower than what has previously been reported to increase T cell proliferation.[35] Interestingly, we also observed that HfMOF-PEG-FA@IMQ uniquely preserved CD4 T cell Ki67 positivity under IR treatment. To assess whether these effects were unique to the tumor, we extend our analysis to the tumor draining lymph nodes and distal lymph nodes (Figure S10, Supporting Information). Collectively, our observations are consistent with previous reports of positive relationships between IRF3/7 activation and tumor-infiltrating immune cell markers in CRC.[36]

3. Conclusion

In this study, we demonstrated that HfMOF-PEG-FA can serve as a radiosensitizing nanocarrier for synergistic antitumor immunotherapy with IMQ. We synthesized HfMOF and modified it with DSPE-PEG-folate with a homogeneous size (~140 nm) for targeted uptake in CRC cells. Intracellular uptake

of HfMOF-PEG-FA increased in CRC cells and inhibited cell proliferation. After combination with IMQ, HfMOF-PEG-FA@IMQ enhanced IR-induced DNA damage and apoptotic and immunogenic cell death, potentially activating type I IFN via IRF signaling *in vitro* and T cell proliferation *in vivo*. Taken together, HfMOF-PEG-FA not only maintains many of the radiosensitizing effects endowed by hafnium IR scattering, but also provides immune-stimulatory properties beyond that of either component alone. Unexpectedly, we discovered that HfMOF upregulates TLR7 expression in CRC, pairing TLR expression with agonism in tumor intrinsic manner. As this was an unexpected occurrence, studies are ongoing to determine molecularly how HfMOFs alone augment TLR expression, but nonetheless our observation provides future directions for the HfMOF platform to exploit TLR expression regulation in combination with radiotherapy and immunotherapy. These features make nanoscale HfMOFs an attractive candidate for further exploration in combination with other therapies including checkpoint blockade.

WILEY-VCH

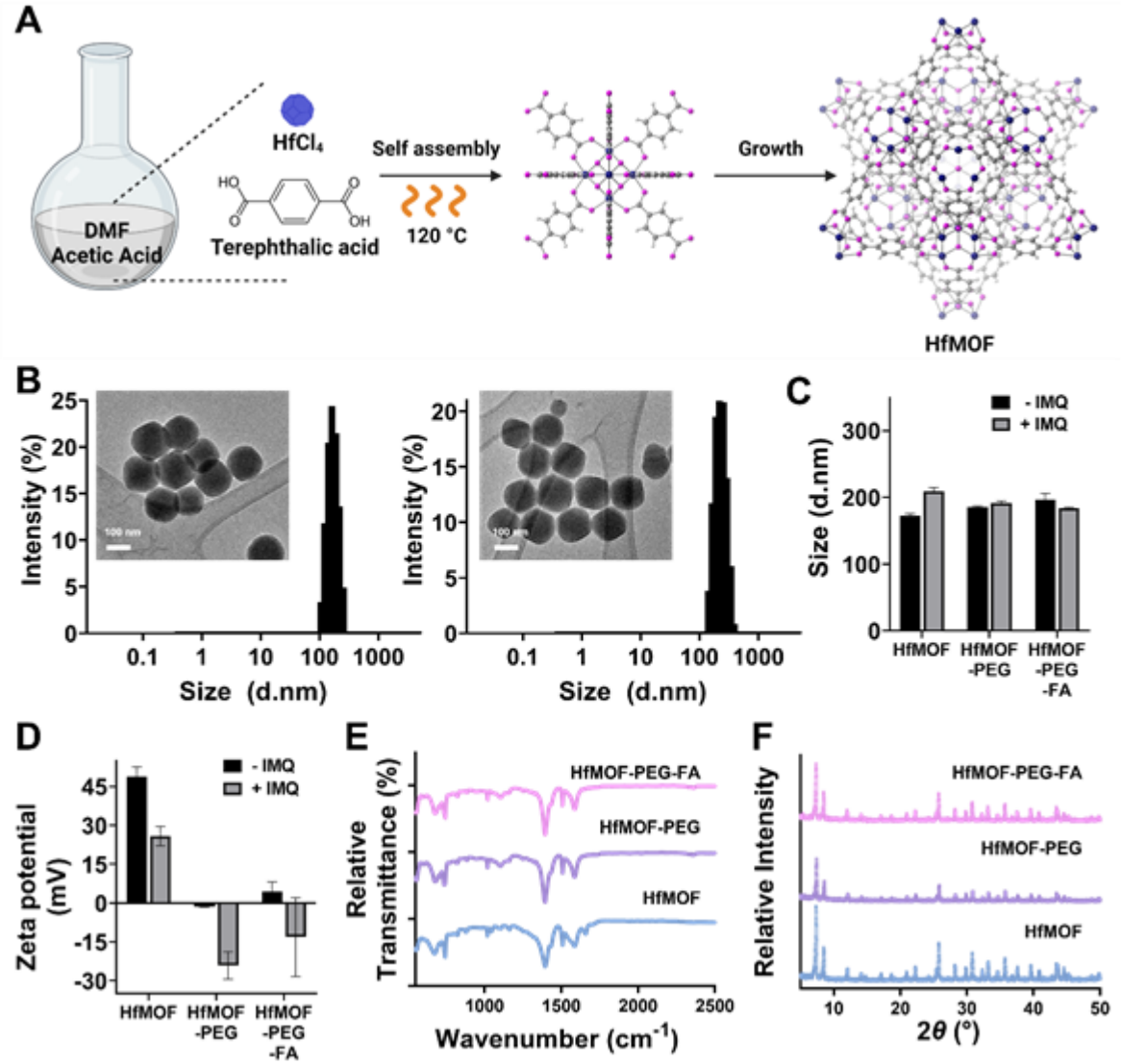

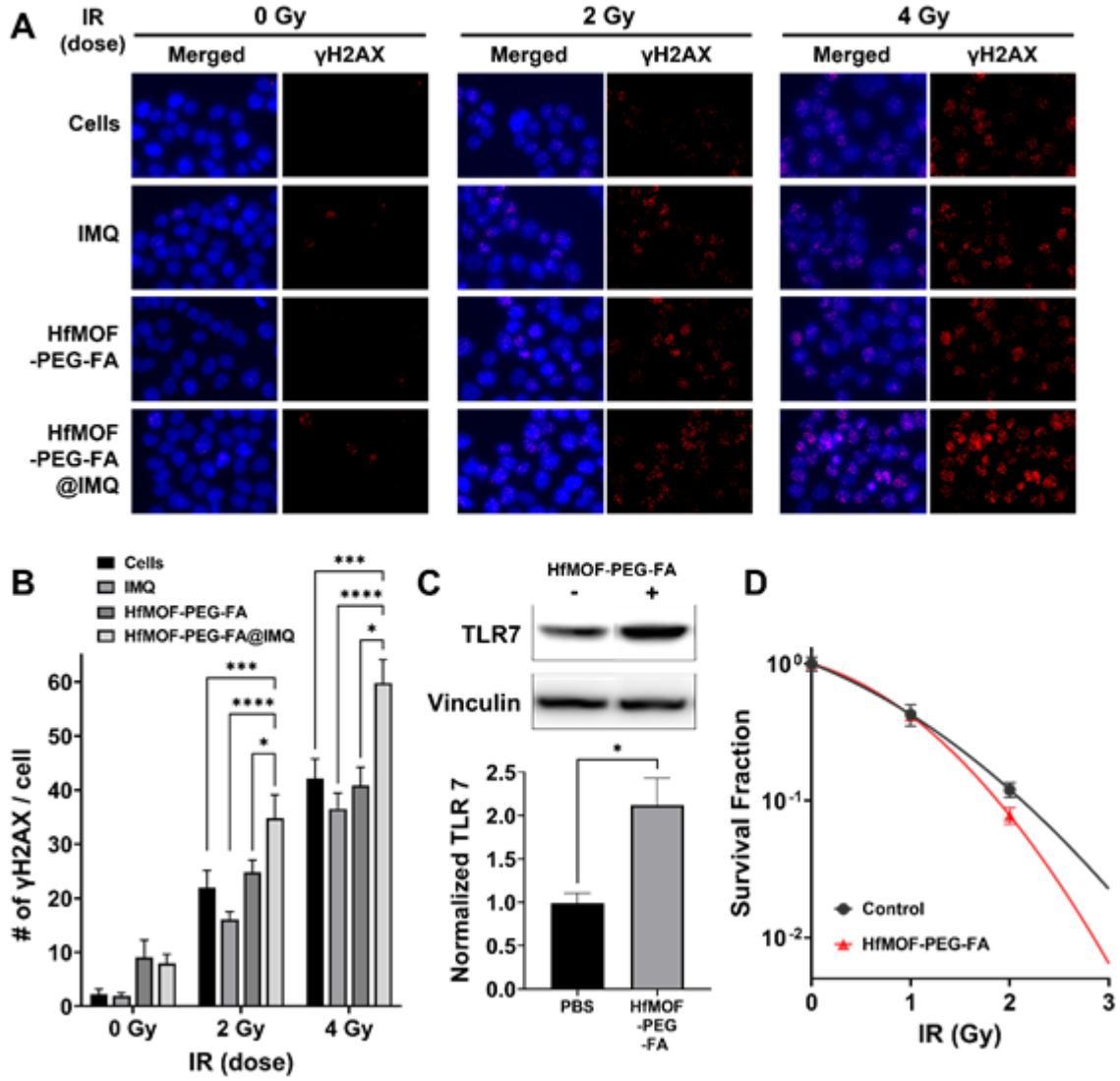

Figure 2.

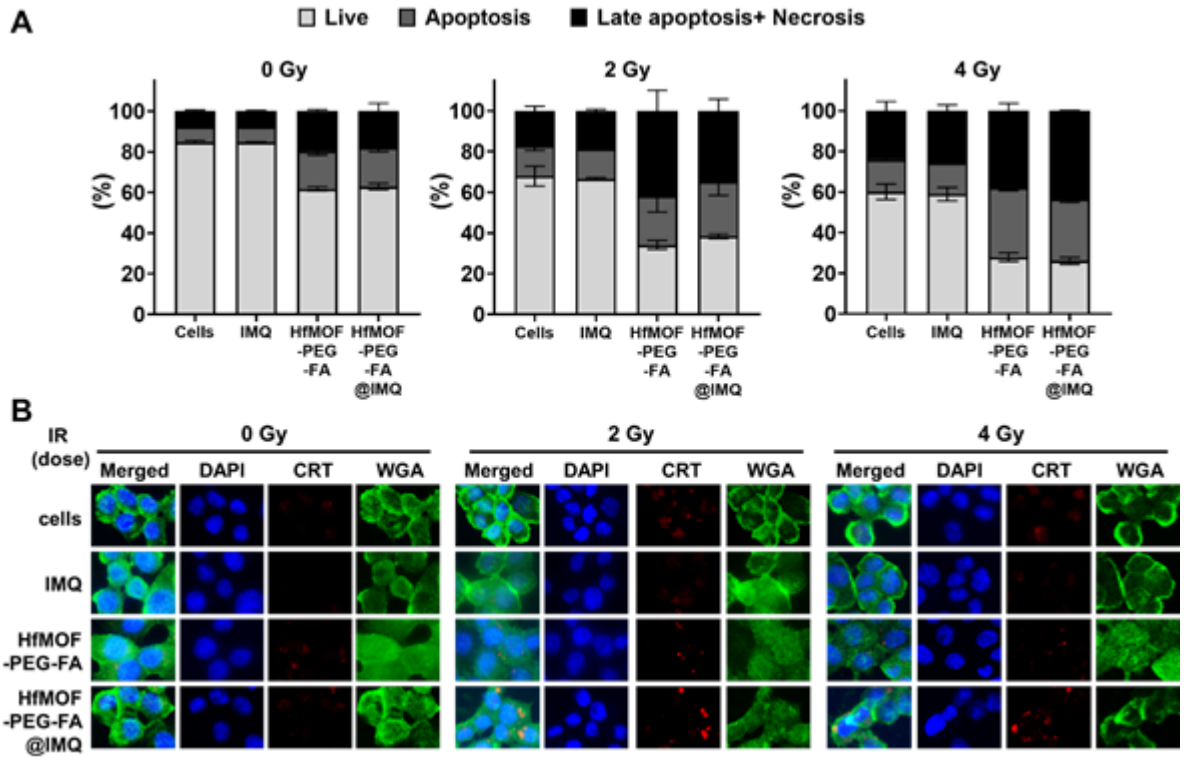

Figure 3.

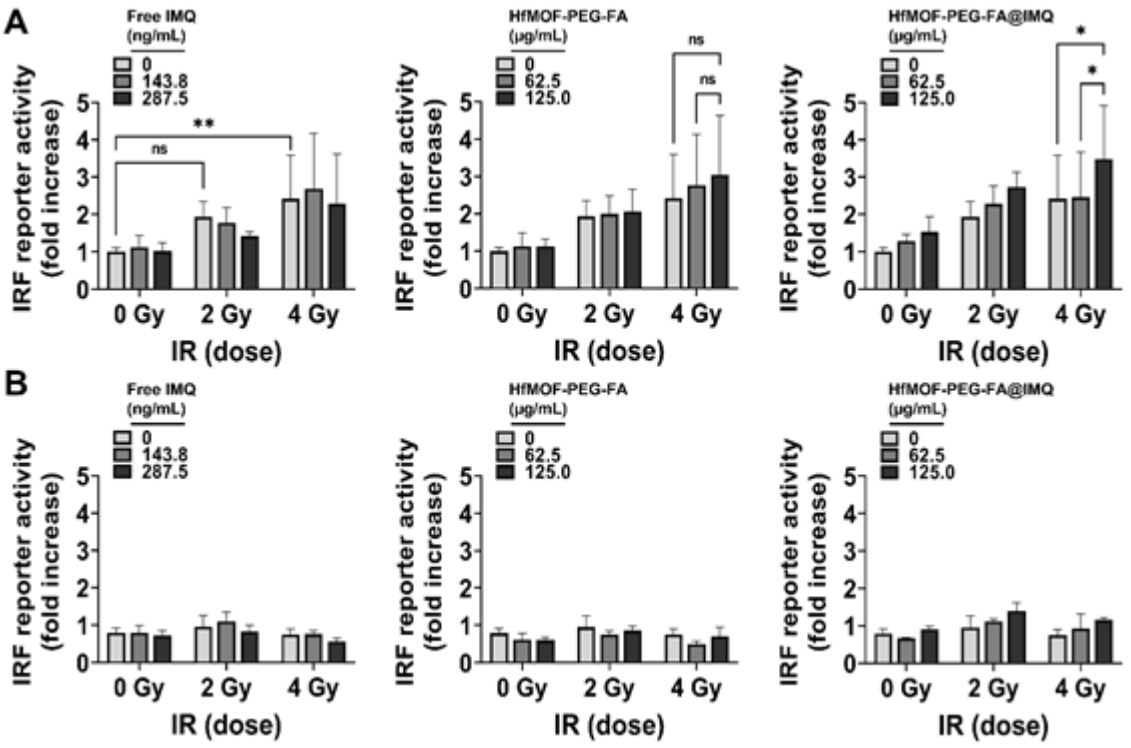

Figure 4.

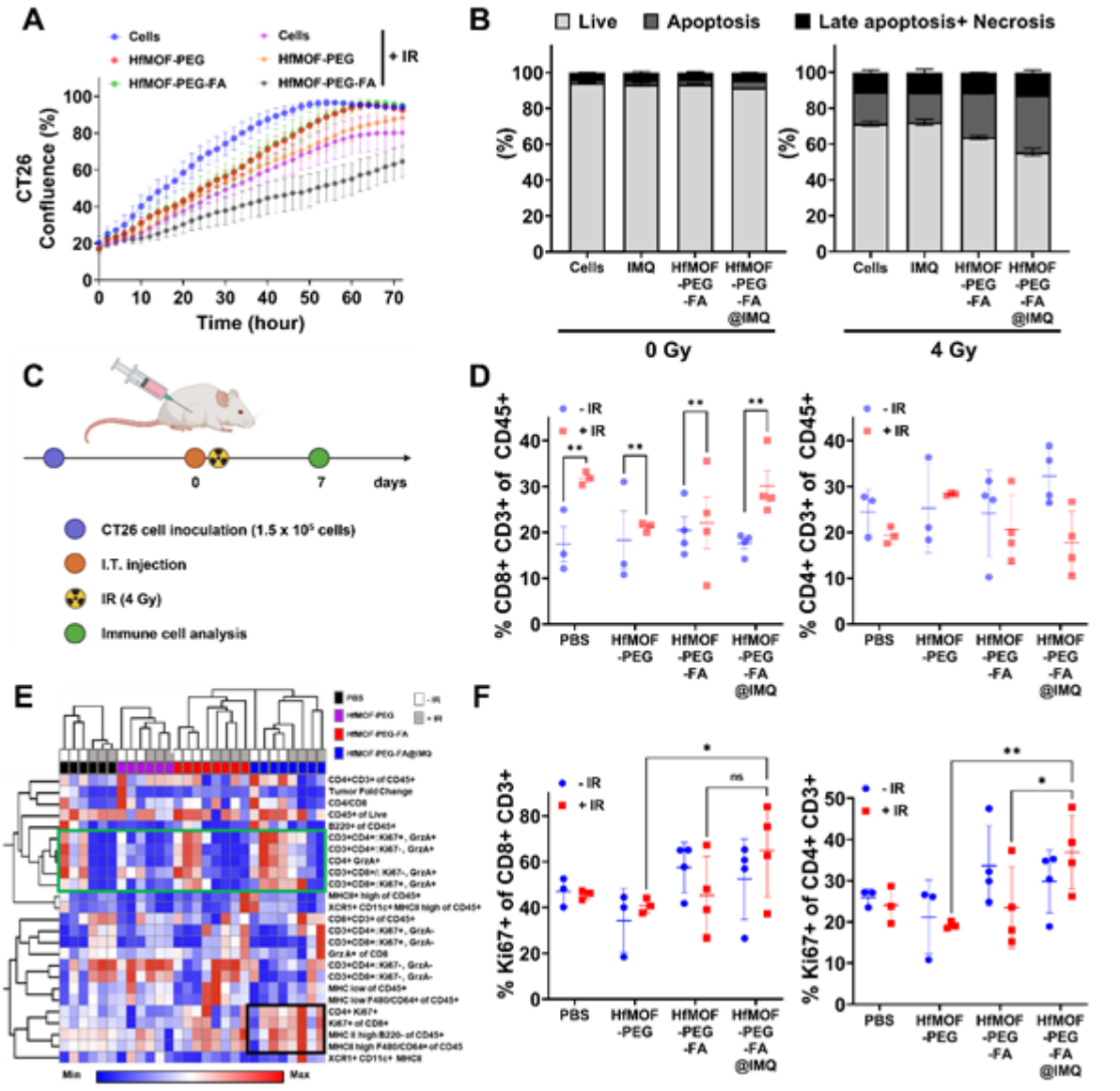

Figure 5.

WILEY-VCH

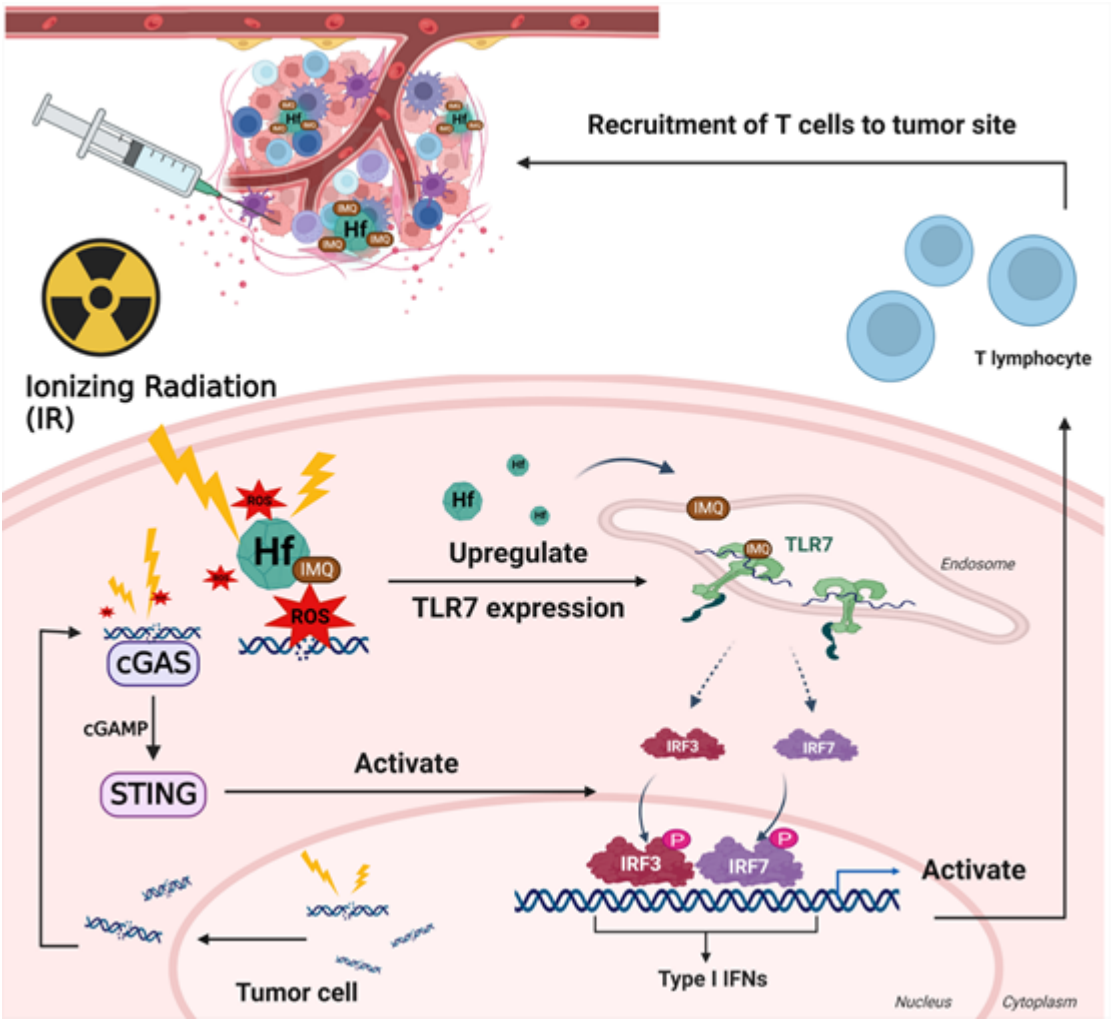

Scheme 1.

Figure 1. Characterization of HfMOF-PEG-FA. (A) Schematic illustration of the synthesis process and crystalline structure of HfMOF-PEG-FA. (B) Size distributions of HfMOF (left panel) and HfMOF-PEG-FA (right panel) from transmission electron microscopy (TEM). Insets: TEM images of each sample, scale bar = 100 nm. (C) Hydrodynamic sizes (n=4-6) and (D) Surface charge of HfMOF, HfMOF-PEG, and HfMOF-PEG-FA before and after IMQ loading (n=2-8). (E) Fourier transform infrared spectra (FT-IR) and (F) X-ray diffraction (XRD) patterns of HfMOF, HfMOF-PEG, and HfMOF-PEG-FA. All data were presented as mean ± SD.

Figure 2. Co-delivery of HfMOF-PEG-FA and IMQ and synergistic cell death mediated by upregulation of TLR7 expression. DNA double-strand breaks by immunohistochemical analysis of γH2AX foci formation. (A) γH2AX puncti visualized within IMQ, HfMOF-PEG-FA, and HfMOF-PEG-FA@IMQ treated HCT116 cells 2 h after irradiation using fluorescence microscope and (B) quantified via CellProfiler analysis. Two-way ANOVA was used for statistical analysis (n=5) (C) TLR7 protein expression quantified by western blot in HCT116 with HfMOF-PEG-FA. One-way ANOVA was used for statistical analysis (n=4). (D) The radiosensitizing activity of HfMOF-PEG-FA assessed by clonogenic assay in HCT116. Colonies of more than 50 cells were counted and plotted as survival fractions by normalizing it to the number of cells plated (n=3). All data were presented as mean ± SD; *$p < 0.05$, ***$p < 0.001$, and ****$p < 0.001$.

Figure 3. (A) Population of radio-activated cell apoptosis analyzed by flow cytometry using Annexin V/PI double staining after treatment with IMQ, HfMOF-PEG-FA, and HfMOF-PEG-FA@IMQ with HCT116 (n=2). (B) Immunogenic cell death monitored by calreticulin exposure on HCT116 cell membrane. Immunofluorescence of calreticulin was stained 4 h after IR with an increasing dose of IR. All data were presented as mean ± SD.

Figure 4. Type I IFN mediated IRF activation in HCT116 triggered by IMQ, HfMOF-PEG-FA, and HfMOF-PEG-FA@IMQ in the presence or absence of IFN receptor inhibitor 96 h after irradiation (A: - IFN receptor inhibitor, B: + IFN receptor inhibitor, n=4-12). All data were presented as mean ± SD. Two-way ANOVA was used for statistical analysis: n.s, not significant; *$p < 0.05$, and **$p < 0.01$.

Figure 5. Radiosensitizing effect of HfMOF-PEG-FA@IMQ on CT26 xenograft model (A) In vitro radiosensitizing activity of HfMOF-PEG-FA assessed by real-time monitoring of cell proliferation of CT26 (B) Population of radio-activated cell apoptosis analyzed by flow cytometry using Annexin V/PI double staining after treatment with IMQ, HfMOF-PEG-FA, and HfMOF-PEG-FA@IMQ with CT26 (C) Schematic illustration of intratumoral administration of HfMOF-PEG-FA@IMQ and analysis of T cells in tumors (D) percentage of CD8 and CD4 T cells in tumors. (E) Flow cytometric analysis of 24 different target cell populations by Euclidean hierarchical clustering in tumor immune cell compositions. (F) proliferation of CD8 and CD4 T cells in tumors (n=3-4). All data were presented as mean ± SD. Two-way ANOVA was used for statistical analysis: n.s, not significant; *$p < 0.05$, and **$p < 0.01$.

Scheme 1. The schematic illustration of synergistic TLR7 mediated cancer radiotherapy of co-delivery of HfMOF-PEG-FA and IMQ for Type I IFN activation. HfMOF-PEG-FA upregulates TLR7 expressions and delivers IMQs to elicit synergistic IRF activation via the STING and TLR pathways and increase the population of proliferating T cells in tumors.

4. Experimental Section

Materials: Acetic acid, acetonitrile, hafnium (IV) chloride ($HfCl_4$, 98+% metals basis excluding Zr), methanol, N,N-dimethylformamide (DMF), and terephthalic acid (BDC) were obtained from Fisher Scientific (Hampton, NH, USA). Imiquimod was purchased from Cayman (Ann Arbor, MI, USA). Dulbecco's phosphate-buffered saline (DPBS) were purchased from Corning Inc (Corning, NY, USA). Dulbecco's modified Eagle's medium (DMEM), Hank's Balanced Salt Solution (HBSS) and penicillin/streptomycin (P/S), Roswell Park Memorial Institute (RPMI) were acquired from Gibco BRL (Grand Island, NY, USA). Fetal bovine serum (FBS) was acquired from Hyclone (Logan, UT, USA). N-(Methylpolyoxyethylene oxycarbonyl)-1,2-distearoyl-sn-glycero-3-phosphoethanolamine, sodium salt (DSPE-PEG) was purchased from NOF America Corporation (San Mateo, CA, USA). 1,2-distearoyl-sn-glycero-3-phosphoethanolamine-N-[folate(polyethylene glycol)-2000] (DSPE-PEG-Folate) was purchased from Nanocs (New York, NY, USA). Anti-human/mouse phospho-H2AX (S139) eFluor® 660, anti-TLR7 polyclonal antibody, and anti-Vinculin recombinant rabbit monoclonal antibody (42H89L44) were obtained from Thermo Fisher Scientific (USA). Goat anti-rabbit IgG (H+L) was purchased from Jackson ImmunoResearch Inc. (West Grove, PA, USA). Anti-calreticulin antibody-ER marker (Alexa Fluor 647) were supplied by Abcam (Cambridge, UK). Prolong diamond antifade

mountant with DAPI, Alexa fluor 488-labeled wheat germ agglutinin (WGA), RBC Lysis Buffer, and LIVE/DEAD Fixable Near-IR Dead Cell Stain Kit were obtained from Invitrogen (Carlsbad, CA, USA). IFNα-IFNAR-IN-1 hydrochloride (HY-12836A) was obtained from MedChemExpress (Monmouth Junction, NJ, USA). Annexin V-FITC kit was purchased from Miltenyi Biotec (Bergisch Gladbach, Germany). HCT116-Dual cells, B16-Blue ISG cells, QUANTI-Blue, and QUANTI-luc assay reagent were obtained from InvivoGen (San Diego, CA, USA). Collagenase type IV and DNase I were purchased from Worthington (Lakewood, NJ, USA).

Formulation of HfMOF-PEG-FA@IMQ: HfMOFs were synthesized as described in our previous study.[17] Briefly, 375 mg of $HfCl_4$ and 268 mg of BDC were added into the round bottom flask and dissolved in 25 mL of DMF. After then, 11 mL of acetic acid and 1.875 mL of deionized water were added in sequence into the round bottom flask. The mixed hafnium solution was heated up to 120 °C for 20 min by stirring in an oil bath. After 20 min, the reacted solution was cooled down to room temperature (RT) and centrifuged for 15 min at 8000 rcf to collect synthesized HfMOF particles. To removed unreacted materials, HfMOF pellets were washed once with DMF and subsequently three times with ethanol via centrifugation at 8000 rcf for 15 min, respectively. The obtained HfMOFs were then dried overnight at 90 °C for further experiments.

To formulate IMQ loaded HfMOF-PEG or HfMOF-PEG-FA (HfMOF-PEG@IMQ or HfMOF-PEG-FA@IMQ), IMQ was firstly loaded into the HfMOF (HfMOF@IMQ), and then DSPE-PEGs or DSPE-PEG-FAs were modified with HfMOF@IMQ. 4 mg of IMQ and 40 mg of HfMOF (10 mg mL^{-1} in MeOH) were added into a glass vial and mixed by sonication at 40 °C for 1 h and subsequently stirred at RT for overnight. To wash out free IMQ, 4 mL of DMSO was added to the vial containing HfMOF@IMQ and the mixed solution was centrifuged at 17000 rcf for 10 min. The HfMOF@IMQ pellets were

additionally washed with MeOH three times to remove residual IMQ and DMSO and centrifuged at 17000 rcf for 10 min and then dried for further modification. To coat DSPE-PEG and DSPE-PEG-FA with HfMOF@IMQ, HfMOF@IMQs were dissolved in MeOH (10 mg mL^{-1}) and reacted with DSPE-PEG (5 mg mL^{-1} in MeOH) or DSPE-PEG-FA (5 mg mL^{-1} in MeOH containing 90% of free DSPE-PEG) at a (DSPE-PEG or DSPE-PEG-FA):HfMOF weight ratio of 1:2 by stirring for 4 h. After PEGylation, MeOH was evaporated with a nitrogen purge, and the dried film of PEGylated HfMOF@IMQs was afterwards resuspended in deionized water. Free DSPE-PEG or DSPE-PEG-FA were removed by washing three times with deionized water via centrifugation at 17000 rcf for 5 min and then freeze-dried. HfMOF-PEG or HfMOF-PEG-FA were prepared by the same method as described above using HfMOF instead of HfMOF@IMQ.

Characterization of HfMOF and HfMOF-PEG-FA@IMQ: The loading amount of IMQ was quantified by Shimadzu SPD-20A high-performance liquid chromatography (HPLC) instrument equipped with an Agilent Zorbax Rapid Resolution SBC-18 column (4.6 mm × 100 mm, 3.5 μm) and a UV/Vis detector and. The detection wavelength of IMQ was set at 320 nm. The mobile phase was acetonitrile:acetate buffer (pH 4.0, 100 mM) (70:30, v/v) and the flow rate was 1.5 mL min^{-1} (31). To prepare a standard curve, IMQ was serially diluted in acetonitrile ranging from 0 to 12.5 μg mL^{-1}, and 10 μL of each standard solution was injected onto the HPLC. The retention time of IMQ in HPLC was approximately 6.3 min, and a calibration plot was prepared in the range of 0-12.5 ng mL^{-1}. To measure the loaded amount of IMQ in HfMOF, supernatant of washed HfMOF@IMQ was injected and unloaded IMQ was quantified using the IMQ standard curve. The hydrodynamic sizes and surface charges of various modified HfMOFs in deionized water were measured by dynamic light scattering (DLS). Additionally, morphology of HfMOF and HfMOF-PEG-FA were examined using a FEI

Tecnai F20 STWIN Transmission Electron Microscope (TEM). Fourier transform infrared spectroscopy (FT-IR) of HfMOF, HfMOF-PEG, and HfMOF-PEG-FA were collected on a Thermo Scientific Nicolet iS10 spectrometer in transmission mode. Powder X-ray diffraction (XRD) patterns were obtained with a Rigaku Ultima IV X-Ray diffractometer using a Cu Kα X-ray source with wide angle powder diffraction.

Clonogenic assay: HCT 116-Dual cells were maintained in DMEM supplemented with 10% FBS, penicillin (100 U mL^{-1}), streptomycin (100 µg mL^{-1}), normocin (100 µg mL^{-1}), blasticidin (10 µg mL^{-1}), and zeocin (100 µg mL^{-1}). All cells were incubated at 37 °C in a humidified atmosphere containing 5% CO_2. HCT 116-Dual cells were plated 24 h prior to treatment at a density of 1×10^6 cells per T25 flask. 125 µg mL^{-1} of HfMOF-PEG and HfMOF-PEG-FA were incubated with cells for 24 h. After the incubation, cells were washed with DPBS and cultured to seed into 6-well plates within the range of 500 to 12000 cells in each well. The plated cells were irradiated with 0, 1, 2, or 4 Gy immediately after seeding and allowed to form colonies for 7 days. Radiation was performed using CellRad Cabinet X-Ray Irradiator (Faxitron, 0.5 mm aluminum filter) operating at 130 kV, 5 mA, 1.2 Gy min^{-1}. The colonies were washed once with DPBS, fixed with 10% formaldehyde, and stained with crystal violet dye (10 µg mL^{-1} in water). Cell survival fractions (%) were determined as follows: the number of colonies/ [the number of plated cells × (plating efficiency/100)]. The colonies with >50 cells were counted and the survival fraction was calculated by dividing the plating efficiency according to the standard procedure.[37]

Monitoring of real-time proliferation: CT26 cells were maintained in RPMI medium supplemented with 10% FBS, penicillin (100 U mL^{-1}), and streptomycin (100 µg mL^{-1}). CT26 was plated into a 48-well plate at a density of 1.5×10^4 cells per well 24 h prior to treatment. Cells were

treated with 125 μg mL^{-1} of HfMOF-PEG and HfMOF-PEG-FA for 24 h. After the incubation, cultured medium was changed with phenol redfree medium and cells were irradiated with 0, 2, and 4 Gy using a CIX2 Cabinet X-Ray Irradiator (Xstrahl, 0.15 mm copper filter) at 160 kV, 18 mA, 1.4 Gy min^{-1}. Irradiated cells were incubated in the IncuCyte Zoom live cell imaging system (Essen BioScience) and monitored every 2 h for a total of 72 h. The confluence of cells was analyzed using the IncuCyte Zoom software.

Immunofluorescence analysis of DNA double-stranded brakes: HCT 116-Dual cells were plated into a poly-L-lysine pre-coated 4-well chamber well 24 h prior to treatment at a density of 5 × 10^4 cells per well. Cells were treated with IMQ (287.5 ng mL^{-1}), HfMOF-PEG-FA (125 μg mL^{-1}), or HfMOF-PEG-FA@IMQ (125 μg mL^{-1}) and incubated for 24 h. After the incubation, cells were irradiated with 0, 2, or 4 Gy using a CIX2 Cabinet X-Ray Irradiator and incubated for another 2 or 4 h. The irradiated cells were washed with DPBS and fixed with 10% formalin for 15 min. Fixed cells were washed using DPBS and then permeabilized and blocked with blocking buffer (5% goat serum with 0.3% Triton X-100 in PBS) for 1 h at RT. Cells were washed twice using DPBS and incubated with 1:100 diluted eFluor 660 conjugated anti-Human/Mouse phospho-H2AX (S139) in dilution buffer (1% BSA with 0.3% Triton X-100 in PBS) for 1 h at RT. Cells were washed three times with DPBS and mounted using ProLong™ Diamond Antifade Mountant with DAPI. The γH2AX in cells was visualized with an EVOS FL Auto microscope and quantified using CellProfiler.

Western blot analysis: HCT 116 cells were plated in a 6-well plate 24 h prior to treatment at a density of 1.5 × 10^5 per well. Cells were treated with HfMOF-PEG-FA (125 μg mL^{-1}) for 4 h and changed with fresh medium for another 20 h incubation. Cells were trypsinized and washed with PBS twice prior to resuspension in RIPA lysis buffer in a microcentrifuge tube. Protein concentrations

were quantified using BCA assay kit and loaded in lanes (20 µg/well) of a 4-12% Tris-Glycine gel. After electrophoresis, gel was transferred to PVDF membrane using iBlot 2 transfer device using P0 method. Membranes were blocked for 1 h at RT in the starting block buffer and incubated overnight at 4 °C with 1:500 diluted TLR7 antibody or 1:1000 diluted vinculin antibody. Horseradish peroxidase conjugated anti-rabbit antibodies was incubated for 1.5 h at RT and western blot detected using chemiluminescent substrate. All raw images for Western blots were included in Supporting Information (Figure S12).

Cell death analysis: HCT 116 cells were seeded into a 6-well plate 24 h prior to treatment at a density of 2×10^5 cells per well. IMQ, HfMOF-PEG-FA, and HfMOF-PEG-FA@IMQ were diluted using cultured media and treated to the cells at an IMQ concentration of 287.5 ng mL^{-1} or HfMOF-PEG-FA concentration of 125 µg mL^{-1} for 24 h. Plates were irradiated with 0, 2, and 4 Gy using a CellRad Cabinet X-Ray Irradiator and then maintained for another 48 h. Cells were collected and stained with Annexin V-FITC/PI according to the manufacturer's protocol for flow cytometry analysis.

Detection of cell surface CRT: HCT 116 cells were plated, treated with IMQ, HfMOF-PEG-FA, or HfMOF-PEG-FA@IMQ, and then irradiated as described above for cellular γH2AX measurement. Cells were placed on ice for 10 min 4 h after the irradiation. Cells were then washed twice with cold DPBS, incubated with 1:500 diluted anti-calreticulin antibody (Alexa Fluor 647), and placed on ice for 1 h. Next, cells were washed twice with cold DPBS and stained with the WGA diluted in HBSS at 5 µg mL^{-1} for 2 min. The stained cells were washed twice using DPBS and fixed with 10% formalin for 10 min. After fixing, cells were washed with DBPS and mounted using ProLong™ Diamond Antifade Mountant with DAPI. The exposed CRT was observed by EVOS FL Auto microscope.

Quantification of IRF activation: HCT 116 cells and B16 cells were seeded in 96-well plates at a density of 2×10^3 cells per well prior to treatment. HfMOF-PEG-FA and HfMOF-PEG-FA@IMQ were diluted with cultured media and added to the cells at different concentrations (0, 62.5, and 125 μg mL^{-1}) in the presence or absence of IFN receptor inhibitor (1 μM). An equal amount of free IMQ in HfMOF-PEG-FA@IMQ was used to treat cells at a range of concentrations (0, 143.8, and 287.5 ng mL^{-1}). After treatment for 24 h, cells were irradiated with 0, 2, or 4 Gy using a CellRad Cabinet X-Ray Irradiator and allowed to incubate for an additional 96 h. Activation of the IRF pathway was confirmed by measuring the activity of Lucia luciferase and secreted embryonic alkaline phosphatase in the cell supernatant. The QUANTI-Luc solution, a Lucia detection reagent, and QUANTI-Blue solution, secreted embryonic alkaline phosphatase detection reagent, were prepared by following the manufacturer's instructions. 50 μL of the QUANTI-Luc solution and 180 μL of the QUANTI-Blue solution were added into each 96-well plate and mixed with 20 μL of supernatant from each well by pipetting gently. The luminescence signal was immediately measured using an Infinite M200 Pro plate reader.

Analysis of proliferating T cells in CT26 tumor model: Female BALB/c mice (6-7 weeks old, Charles River Laboratories, Wilmington, MA) were inoculated with CT26 cells (1.5×10^5 cells) subcutaneously into the right flank. All animal care and experimental procedures were approved by the Institutional Animal Care and Use Committee (IACUC, protocol # TR02_IP00000023) of Oregon Health and Sciences University. When the average size of the tumors reached ~50 mm^3, mice were intratumorally injected with PBS, HfMOF-PEG-FA, or HfMOF-PEG-FA@IMQ at a Hf dose of 2.25 ng kg^{-1}, after anesthetizing with isoflurane. After 4 h of administration, the tumors were irradiated with 4 Gy using a CIX2 Cabinet X-Ray Irradiator and harvested on day 7 post-treatment for T cell analysis.

Tumors were cut into small fragments and digested with 1 mg mL^{-1} collagenase and 100 μg mL^{-1} deoxyribonuclease in RPMI medium for 20 min at 37 °C in 5% CO_2 incubator, and then treated with 100 mM EDTA in PBS at a final concentration of 15 mM EDTA for another 10 min at 37°C in 5% CO_2 incubator. Subsequently, the digested tumors were ground using the rubber end of a syringe and filtered through a 70 μm nylon mesh filter to collect single cells. Cells were washed using flow wash buffer (PBS containing 2 mM EDTA and 0.5% BSA) and collected by centrifugation at 450 rcf for 5 min at 4°C. The pelleted cells were resuspended in RBC lysis buffer on ice for 10 min and quenched with the addition of cold 5 mM EDTA in PBS. After washing, 1×10^6 cells were stained with live dead cell staining dye and then incubated with anti-CD16/32 (Clone:93, BioLegend). Cells were further stained with the following fluorochrome conjugated antibodies: CD8α Super Bright 645 (Clone: 53-6.7, eBioscience), CD4 Brilliant Violet 711 (Clone: H129.19, BD Biosciences), MHCII BUV563 (Clone: M5/114.15.2, BD Biosciences), CD45R/B220 BUV805 (Clone: RA3-6B2, BD Biosciences), CD3 Alexa Fluor 700 (Clone: H57-597, BioLegend), Granzyme A PE-Cyanine7 (Clone: GzA-3G8.5, eBioscience), CD64 PerCP-eFluor™ 710 (Clone: X54-5/7.1, eBioscience), XCR1 Brilliant Violet 785 (Clone: ZET, BioLegend), CD11c BUV737 (Clone: N418, BD Biosciences), F4/80 PE-eFluor™ 610 (Clone: BM8, eBioscience), Ki-67 eFluor™ 506 (Clone: SolA15, eBioscience), and CD45-BUV395 (Clone: 30-F11, BD Horizon™). The stained cells were analyzed using Cytek Aurora. Gating strategy for flow cytometry analysis was shown in Supporting Information (Figure S11). Hierarchical clustering was performed using Morpheus (https://software.broadinstitute.org/morpheus) with Euclidean distances calculated by average linkage. Visualization was performed with columns group by treatment and clustering permitted for IR treatment and all rows of immunological parameters. Figure 5E and Figure S10 were generated with fixed column locations and clustering permitted by rows.

Statistical Analysis: All data were analyzed using the GraphPad Prism software and presented as mean ± standard deviations (SD). One- or two-way ANOVA were used to evaluate the significant differences between two or multiple groups. Statistical significance is denoted by *p < 0.05, **p < 0.01, ***p < 0.001, and ****p < 0.001.

Supporting Information

Supporting Information is available from the Wiley Online Library or from the author.

Acknowledgements

This work was supported by NIH NIGMS as a Maximizing Investigators' Research Award R35GM119839 (C.S.). The authors thank Rachel Nguyen and Elaine Huang in Walker lab at OHSU for their assistance with IncuCyte analysis and animal studies in this study.

Received: ((will be filled in by the editorial staff))

Revised: ((will be filled in by the editorial staff))

Published online: ((will be filled in by the editorial staff))

References

[1] Y. Liu, P. Zhang, F. Li, X. Jin, J. Li, W. Chen, Q. Li, *Theranostics* **2018**, *8*, 1824.

[2] Y. Xie, Y. Han, X. Zhang, H. Ma, L. Li, R. Yu, H. Liu, *Front Oncol* **2021**, *11*, 633827.

[3] a)S. Bonvalot, P. L. Rutkowski, J. Thariat, S. Carrere, A. Ducassou, M. P. Sunyach, P. Agoston, A. Hong, A. Mervoyer, M. Rastrelli, V. Moreno, R. K. Li, B. Tiangco, A. C. Herraez, A. Gronchi, L. Mangel, T. Sy-Ortin, P. Hohenberger, T. de Baere, A. Le Cesne, S. Helfre, E. Saada-Bouzid, A. Borkowska, R. Anghel, A. Co, M. Gebhart, G. Kantor, A. Montero, H. H. Loong, R. Verges, L. Lapeire, S. Dema, G. Kacso, L. Austen, L. Moureau-Zabotto, V. Servois, E. Wardelmann, P. Terrier, A. J. Lazar, J. Bovee, C. Le Pechoux, Z. Papai, *Lancet Oncol* **2019**, *20*, 1148; b)C. Hoffmann, V. Calugaru, E. Borcoman, V. Moreno, E. Calvo, X. Liem, S. Salas, B. Doger, T. Jouffroy, X. Mirabel, J. Rodriguez, A. Chilles, K. Bernois, M. Dimitriu, N. Fakhry, S. W. Hee Kam, C. Le Tourneau, *Eur J Cancer* **2021**, *146*, 135.

[4] a)M. H. Chen, N. Hanagata, T. Ikoma, J. Y. Huang, K. Y. Li, C. P. Lin, F. H. Lin, *Acta Biomater* **2016**, *37*, 165; b)K. Ni, T. Luo, G. T. Nash, W. Lin, *Acc Chem Res* **2020**, *53*, 1739.

[5] K. Ni, G. Lan, N. Guo, A. Culbert, T. Luo, T. Wu, R. R. Weichselbaum, W. Lin, *Sci Adv* **2020**, *6*.

[6] E. Mladenov, S. Magin, A. Soni, G. Iliakis, *Front Oncol* **2013**, *3*, 113.

[7] R. X. Huang, P. K. Zhou, *Signal Transduct Target Ther* **2020**, *5*, 60.

[8] a)L. Deng, H. Liang, M. Xu, X. Yang, B. Burnette, A. Arina, X. D. Li, H. Mauceri, M. Beckett, T. Darga, X. Huang, T. F. Gajewski, Z. J. Chen, Y. X. Fu, R. R. Weichselbaum, *Immunity* **2014**, *41*, 843; b)H. J. Chon, H. Kim, J. H. Noh, H. Yang, W. S. Lee, S. J. Kong, S. J. Lee, Y. S. Lee, W. R. Kim, J. H. Kim, G. Kim, C. Kim, *J Cancer* **2019**, *10*, 4932.

[9] a)T. Xia, H. Konno, J. Ahn, G. N. Barber, *Cell Rep* **2016**, *14*, 282; b)L. Corrales, T. F. Gajewski, *Clin Cancer Res* **2015**, *21*, 4774.

[10] a)J. Constanzo, J. Faget, C. Ursino, C. Badie, J. P. Pouget, *Front Immunol* **2021**, *12*, 680503; b)L. Motedayen Aval, J. E. Pease, R. Sharma, D. J. Pinato, *J Clin Med* **2020**, *9*.

[11] a)T. Su, Y. Zhang, K. Valerie, X. Y. Wang, S. Lin, G. Zhu, *Theranostics* **2019**, *9*, 7759; b)G. N. Barber, *Nat Rev Immunol* **2015**, *15*, 760.

[12] a)N. O. Gekara, *J Cell Biol* **2017**, *216*, 2999; b)K. J. Mackenzie, P. Carroll, C. A. Martin, O. Murina, A. Fluteau, D. J. Simpson, N. Olova, H. Sutcliffe, J. K. Rainger, A. Leitch, R. T. Osborn, A. P.

Wheeler, M. Nowotny, N. Gilbert, T. Chandra, M. A. M. Reijns, A. P. Jackson, *Nature* **2017**, *548*, 461; c)J. Marill, N. Mohamed Anesary, S. Paris, *Radiother Oncol* **2019**, *141*, 262.

[13] a)E. S. Choi, J. Song, Y. Y. Kang, H. Mok, *Macromol Biosci* **2019**, *19*, e1900042; b)E. J. Mifsud, A. C. Tan, D. C. Jackson, *Front Immunol* **2014**, *5*, 79.

[14] a)J. H. Cho, H. J. Lee, H. J. Ko, B. I. Yoon, J. Choe, K. C. Kim, T. W. Hahn, J. A. Han, S. S. Choi, Y. M. Jung, K. H. Lee, Y. S. Lee, Y. J. Jung, *Oncotarget* **2017**, *8*, 24932; b)M. Schon, A. B. Bong, C. Drewniok, J. Herz, C. C. Geilen, J. Reifenberger, B. Benninghoff, H. B. Slade, H. Gollnick, M. P. Schon, *J Natl Cancer Inst* **2003**, *95*, 1138.

[15] X. Cen, S. Liu, K. Cheng, *Front Pharmacol* **2018**, *9*, 878.

[16] C. Guiducci, R. L. Coffman, F. J. Barrat, *J Intern Med* **2009**, *265*, 43.

[17] M. J. Neufeld, A. N. DuRoss, M. R. Landry, H. Winter, A. M. Goforth, C. Sun, *Nano Research* **2019**, *12*, 3003.

[18] Z. C. Soe, B. K. Poudel, H. T. Nguyen, R. K. Thapa, W. Ou, M. Gautam, K. Poudel, S. G. Jin, J. H. Jeong, S. K. Ku, H. G. Choi, C. S. Yong, J. O. Kim, *Asian J Pharm Sci* **2019**, *14*, 40.

[19] a)A. Wani, G. H. L. Savithra, A. Abyad, S. Kanvinde, J. Li, S. Brock, D. Oupicky, *Sci Rep* **2017**, *7*, 2274; b)S. J. Soenen, W. J. Parak, J. Rejman, B. Manshian, *Chem Rev* **2015**, *115*, 2109.

[20] J. Che, C. I. Okeke, Z. B. Hu, J. Xu, *Curr Pharm Des* **2015**, *21*, 1598.

[21] C. B. Rodell, S. P. Arlauckas, M. F. Cuccarese, C. S. Garris, R. Li, M. S. Ahmed, R. H. Kohler, M. J. Pittet, R. Weissleder, *Nat Biomed Eng* **2018**, *2*, 578.

[22] S. Bhagchandani, J. A. Johnson, D. J. Irvine, *Adv Drug Deliv Rev* **2021**, *175*, 113803.

[23] A. J. Wagstaff, C. M. Perry, *Drugs* **2007**, *67*, 2187.

[24] S. Fletcher, K. Steffy, D. Averett, *Curr Opin Investig Drugs* **2006**, *7*, 702.

[25] a)K. Ni, T. Luo, A. Culbert, M. Kaufmann, X. Jiang, W. Lin, *J Am Chem Soc* **2020**, *142*, 12579; b)S. K. Ramineni, L. L. Cunningham, Jr., T. D. Dziubla, D. A. Puleo, *J Pharm Sci* **2013**, *102*, 593.

[26] L. Maggiorella, G. Barouch, C. Devaux, A. Pottier, E. Deutsch, J. Bourhis, E. Borghi, L. Levy, *Future Oncol* **2012**, *8*, 1167.

[27] J. Fucikova, O. Kepp, L. Kasikova, G. Petroni, T. Yamazaki, P. Liu, L. Zhao, R. Spisek, G. Kroemer, L. Galluzzi, *Cell Death Dis* **2020**, *11*, 1013.

[28] M. Feng, J. Y. Chen, R. Weissman-Tsukamoto, J. P. Volkmer, P. Y. Ho, K. M. McKenna, S. Cheshier, M. Zhang, N. Guo, P. Gip, S. S. Mitra, I. L. Weissman, *Proc Natl Acad Sci U S A* **2015**, *112*, 2145.

[29] N. G. Medvedeva, I. V. Panyutin, I. G. Panyutin, R. D. Neumann, *Radiat Res* **2007**, *168*, 493.

[30] R. Shen, D. Liu, X. Wang, Z. Guo, H. Sun, Y. Song, D. Wang, *Front Cell Dev Biol* **2021**, *9*, 828657.

[31] T. J. Hayman, M. Baro, T. MacNeil, C. Phoomak, T. N. Aung, W. Cui, K. Leach, R. Iyer, S. Challa, T. Sandoval-Schaefer, B. A. Burtness, D. L. Rimm, J. N. Contessa, *Nat Commun* **2021**, *12*, 2327.

[32] a)C. Vanpouille-Box, A. Alard, M. J. Aryankalayil, Y. Sarfraz, J. M. Diamond, R. J. Schneider, G. Inghirami, C. N. Coleman, S. C. Formenti, S. Demaria, *Nat Commun* **2017**, *8*, 15618; b)A. Antonczyk, B. Krist, M. Sajek, A. Michalska, A. Piaszyk-Borychowska, M. Plens-Galaska, J. Wesoly, H. A. R. Bluyssen, *Front Immunol* **2019**, *10*, 1176.

[33] C. E. Samuel, *Clin Microbiol Rev* **2001**, *14*, 778.

[34] a)T. Ilg, *Mol Immunol* **2017**, *90*, 182; b)B. B. Jutte, C. Krollmann, K. Cieslak, R. M. Koerber, P. Boor, C. M. Graef, E. Bartok, M. Wagner, T. Carell, J. Landsberg, P. Aymans, J. Wenzel, P. Brossart, L. L. Teichmann, *iScience* **2021**, *24*, 102833; c)D. Shae, K. W. Becker, P. Christov, D. S. Yun, A. K. R. Lytton-Jean, S. Sevimli, M. Ascano, M. Kelley, D. B. Johnson, J. M. Balko, J. T. Wilson, *Nat Nanotechnol* **2019**, *14*, 269.

[35] a)D. Richardt-Pargmann, M. Wechsler, A. M. Krieg, J. Vollmer, M. Jurk, *Immunobiology* **2011**, *216*, 12; b)S. W. Huang, S. T. Wang, S. H. Chang, K. C. Chuang, H. Y. Wang, J. K. Kao, S. M. Liang, C. Y. Wu, S. H. Kao, Y. J. Chen, J. J. Shieh, *J Invest Dermatol* **2020**, *140*, 1771.

[36] Y. J. Chen, S. N. Luo, L. Dong, T. T. Liu, X. Z. Shen, N. P. Zhang, L. Liang, *J Transl Med* **2021**, *19*, 379.

[37] N. A. Franken, H. M. Rodermond, J. Stap, J. Haveman, C. van Bree, *Nat Protoc* **2006**, *1*, 2315.

WILEY-VCH

C. Author 2, D. E. F. Author 3, A. B. Corresponding Author*

*Eunseo Choi, Madeleine Landry, Nathan Pennock, Megan Neufeld, Katherine Weinfurter, Andrea Goforth, Joshua Walker, and Conroy Sun**

Title

Nanoscale hafnium metal-organic frameworks enhance radiotherapeutic effects by upregulation of type I interferon and TLR7 expression

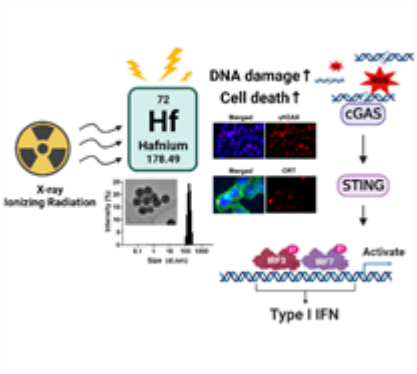

A folate modified hafnium-containing metal organic framework successfully delivers Imiquimod, a TLR7 agonist, into colorectal cancer cells. This combination platform performs as a radiosensitizing nanocarrier for synergistic antitumor immunotherapy by enhancing DNA double-stranded breaks and cell death, including apoptosis, necrosis, and calreticulin exposure, in response to X-ray irradiation and promoting IRF stimulation within tumor cells.